Tomography of Materials and Structures 4 (2024) 100023

Contents lists available at ScienceDirect

Tomography of Materials and Structures

journal homepage: www.journals.elsevier.com/tomography-of-materials-and-structures

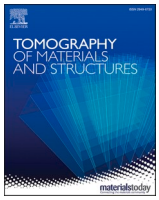

evoSegment: 4D image segmentation of microstructural evolution using joint histograms

Johan Hektor [a,*], Jonas Engqvist [b], Stephen A. Hall [b]

[a] Department of Materials Science and Applied Mathematics, Malmö University, 205 06 Malmö, Sweden
[b] Division of Solid Mechanics, Lund University, Ole Römers Väg 1, 223 63 Lund, Sweden

ARTICLE INFO

Keywords:
Image segmentation
4D evolution
Clustering

ABSTRACT

A method for semantic segmentation of microstructure evolution from 4D imaging data is described and demonstrated. The method is based on a joint histogram describing the time history of the grayscale in each voxel of the images. After identifying and labeling clusters in the joint histogram, the labels are mapped back to the image. The results demonstrate accurate segmentation and characterization of sample evolution. The advantages of the proposed method include automatic segmentation of many time steps and the ability to track grayscale evolution over time and thereby discriminate similar evolution in different material phases. The method is demonstrated through application to 4D X-ray tomography datasets of temperature cycling in cement mortar and tensile testing of a cast iron sample. Water and air exchange in a pore inside the cement mortar is successfully segmented as a function of temperature. In the case of the deforming cast iron sample, several damage mechanisms are identified and segmented. The method is implemented in an open-source Python package called *evoSegment*.

1. Introduction

Owing to recent technological advancements and scientific breakthroughs, in situ experiments with 3D imaging using X-ray and neutron tomography have witnessed a surge in popularity across various fields, including additive manufacturing [1], batteries [2–4], biomechanics [5–7], food science [8], packaging materials [9,10], and geomechanics [11,12]. In this context, image segmentation is pivotal in the data analysis pipeline. Accurate segmentation allows meaningful information to be extracted from image data, facilitating precise and accurate studies of evolving processes. A large number of image segmentation methods have been developed to tackle the challenge of semantic segmentation, i.e., the categorization of pixels in an image into classes. Traditional thresholding methods, such as the widely used Otsu's method [13], classify pixels relative to a threshold value, thereby separating objects from the background. Edge-detection methods, often based on the Canny method [14], identify and segment objects by detecting their boundaries. In clustering algorithms, pixels are grouped into clusters based on similarity measures, e.g., the Euclidean distance, providing a flexible approach for image segmentation and enabling instance segmentation, i.e., labeling individual objects in a given class. In recent years, a multitude of segmentation methods based on artificial intelligence have emerged (e.g., [15–17]), leveraging the power of machine learning and deep learning techniques.

This paper introduces a novel method for semantic segmentation of 4D images to classify objects and their evolution from sequences of images using a clustering approach based on a joint histogram. A conceptually similar, but much less general, approach was taken in Ref. [18] for the specific case of segmenting water and fibers in yarn samples. We provide a detailed description of the segmentation method, highlighting its key components and underlying principles. Furthermore, we demonstrate the applicability and effectiveness of the method on a diverse set of real and synthetic datasets, showcasing its accuracy and robustness. In particular, the method is suitable for segmenting 4D (3D + time) tomography data of evolving samples. The main advantages of the proposed method are: .

- Automatic segmentation of all images in a time series (4D segmentation): The method can segment all images in a time sequence based on labeling only one joint histogram. This can dramatically decrease the data analysis time for 4D datasets with a large number of timesteps.

* Corresponding author.
E-mail address: johan.hektor@mau.se (J. Hektor).

https://doi.org/10.1016/j.tmater.2023.100023
Received 2 November 2023; Received in revised form 13 December 2023; Accepted 13 December 2023
Available online 15 December 2023

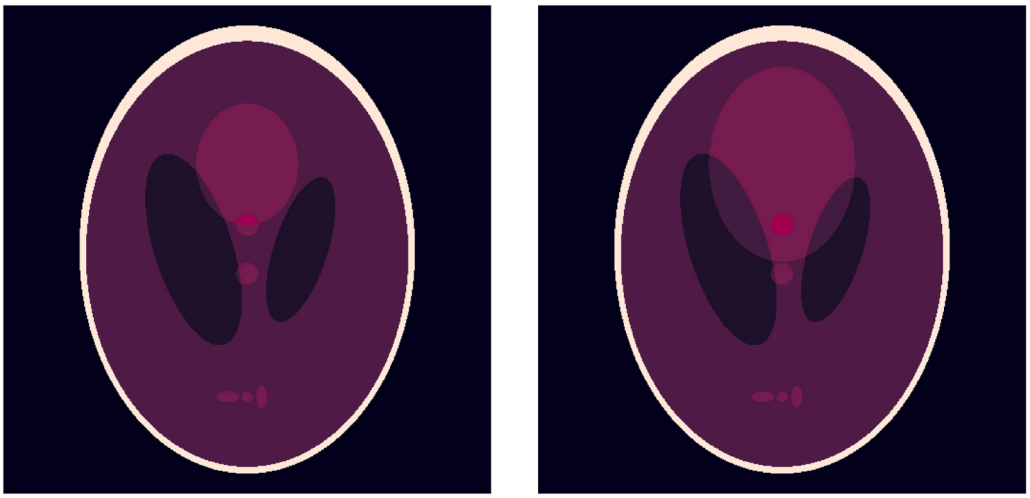

(a) (b)

Fig. 1. (a): Shepp-Logan phantom in the reference state. (b): Shepp-Logan phantom in the evolved state after one of the ellipses grows.

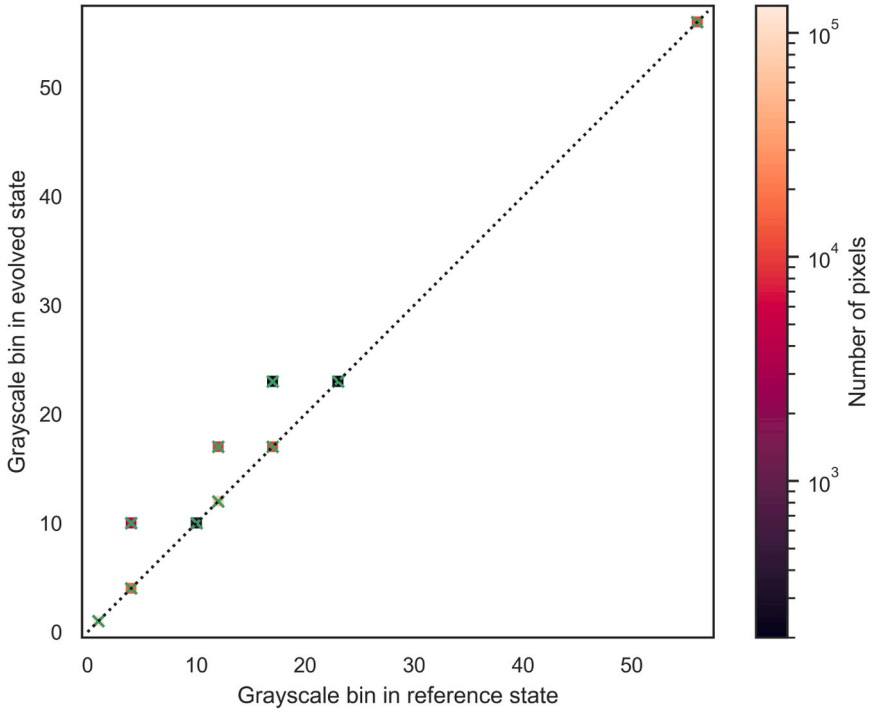

Fig. 2. Joint histogram of the Shepp-Logan phantom images. The grayscale in the reference state is along the horizontal axis, and the grayscale in the evolved state is along the vertical axis. The green crosses correspond to the cluster positions determined by the *diagonal peak extraction* algorithm. The dotted line corresponds to the main diagonal of the joint histogram.

- Memory efficiency: One major problem with imaging data is that the datasets often are too large to fit in the memory of the computer. In the proposed algorithm, the segmentation is done on the joint histogram (i.e., a single 2D image) rather than on the raw data. The images are only needed to construct the histogram and map the labels back to the volume. If needed, both of these tasks can be performed sequentially on small subvolumes of the data that fit in memory.
- Ability to discriminate between phases of similar gray levels: The 2D nature of the joint histogram means that the likelihood of accurately separating two phases with similar grayscale increases.
- Tracking of the origin of the grayscale evolution: The method takes the time history of the grayscale for each voxel into account. This means that the proposed algorithm will accurately separate them even if two different types of sample evolution give the same grayscale in the final state. In conventional thresholding methods, the time history is not kept. Therefore, such methods fail to separate the two materials in the final image and so will also not capture the different types of material evolution.

An open-source python package implementing the method is available.[1]

[1] https://pypi.org/project/evosegment/or https://gitlab.com/jhektor/evoSegment/

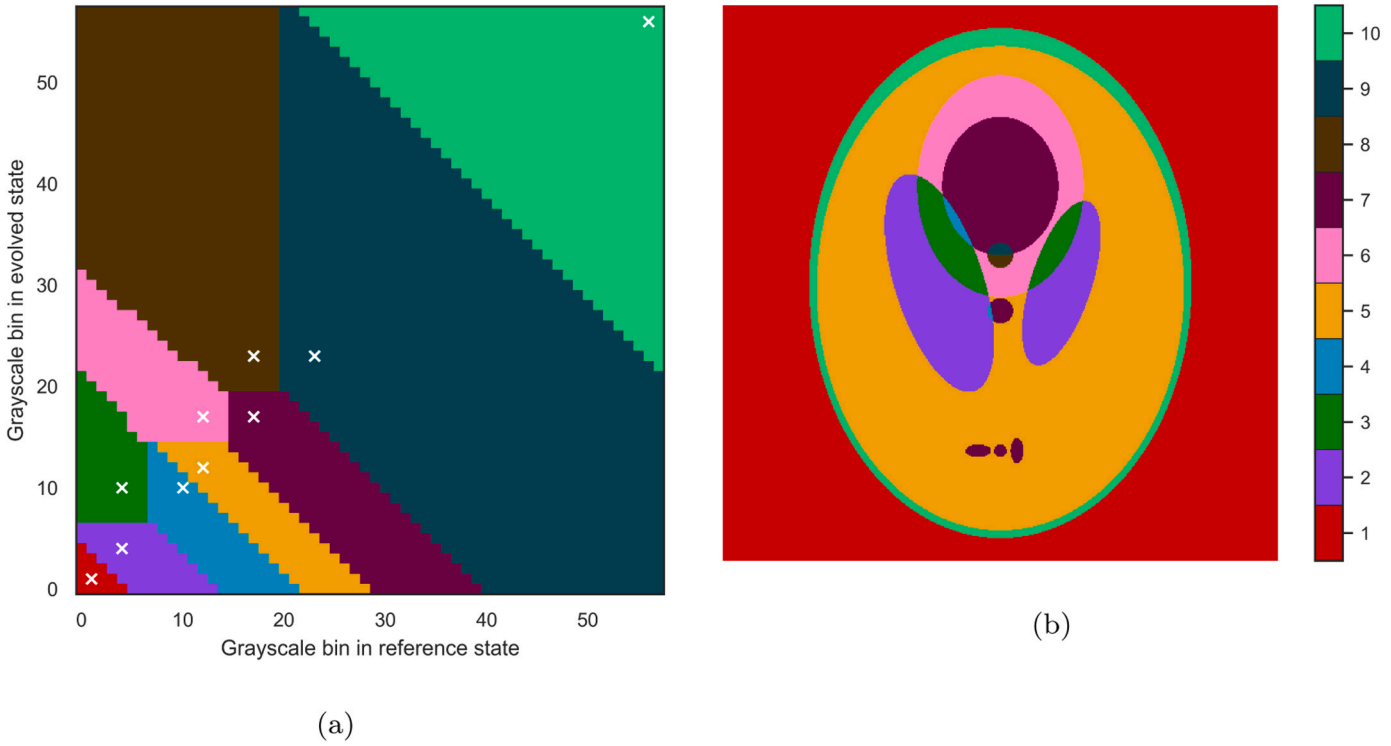

Fig. 3. (a): Labeled joint histogram. The white crosses represent the center-of-mass position of the labels. (b): Image segmentation based on the joint histogram.

2. Segmentation method

To illustrate the segmentation algorithm, we use the Shepp-Logan phantom [19] shown in Fig. 1. The phantom consists of six discrete grayscale values or phases. We consider the standard version of the phantom (Fig. 1a) and an evolved version where the central ellipse has grown significantly (Fig. 1b). The segmentation aims to characterize this growth relative to the reference state by separating the ellipse pixels that were initially part of the large dark regions from those originally part of the small circular regions. In real applications, such grayscale evolution could relate to, e.g., tumor growth [20], fluid flow [21–24], crack propagation [25–27], lithiation in Li-ion batteries [28], or numerous other phenomena. The steps in the proposed segmentation method are described below.

2.1. Prerequisites for the method to work

The main tool in the method is a joint histogram of the pixel intensities in two images, one in a reference state and the other in an evolved state, as described below. A similar approach has previously been used for overlapping 3D volumes from X-ray and neutron tomography of the same object [29–32]. The interpretation of the joint histogram for segmentation relies on the images being registered in space such that the same pixel (voxel) in each image corresponds to the same position in the sample. Such registration can be achieved through various methods, e.g., based on digital image/volume correlation (DIC or DVC) [31,33,34].

Table 1
Interpretation of the segmentation in Fig. 3b.

Label	Interpretation
1	Background.
2	Parts of the large inclined ellipses unaffected by the growing ellipse.
3	Part of the growing ellipse that has expanded into the large inclined ellipses.
4	Small regions where the left inclined ellipse overlaps with the small central circle and the growing ellipse.
5	Unchanged region in the interior of the object.
6	The growth of the central ellipse in the interior of the object.
7	Original region of the growing ellipse, the lower of the small central ellipses, and the three ellipses in the lower part of the image.
8	Part of the upper small central ellipse covered by the growing ellipse during evolution.
9	Non-evolved part of the upper small central ellipse.
10	Outer border of the object.

2.2. Properties of the joint histogram

The joint histogram of the phantoms in Fig. 1 is shown in Fig. 2. In this histogram, the grayscale values of the image in the reference and evolved states are binned along the horizontal and vertical axes, respectively. Given the discrete values in the phantom images, most of the histogram is empty. For actual experimental data, however, this may not necessarily be the case (cf. section 3 for examples of joint histograms from real data). The segmentation algorithm will, nevertheless, be the same for discrete and continuous histograms.

In scenarios where no gray-level evolution occurs (i.e., the image in the evolved state is identical to the image in the reference state), all voxels will be in bins along the diagonal of the histogram. Consequently, regions of the image that show no evolution will always appear along the diagonal. The seven diagonal bins in Fig. 2 correspond to the six discrete phases in the phantom and the background. Any evolution of the grayscale in the evolved state will manifest in the histogram as off-diagonal clusters. By construction of the joint histogram, regions that become darker in the evolved image will cluster below the diagonal, and brightening regions will cluster above the diagonal. In the example of the phantom, the growth of the central ellipse results in an increase in the grayscale value within some regions of three of the phases, thus forming the three bins above the main diagonal in the histogram. Three of the phases and the background of Fig. 1 remain unaffected; therefore, no off-diagonal clusters are formed from them.

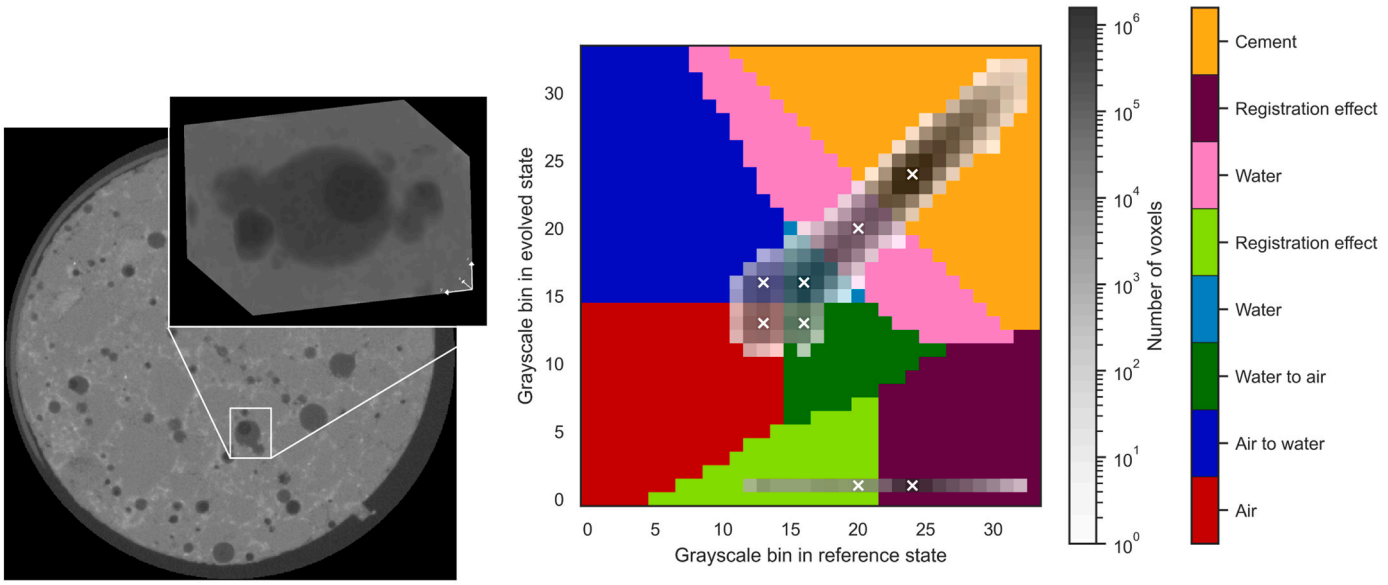

Fig. 4. (a): Slice through the cement mortar sample. The annotation indicates the approximate bounding box of the subvolume that was segmented. The inset shows a 3D rendering of the subvolume. (b): Labeled joint histogram of the subvolume containing a pore. The white crosses represent the final cluster positions. The gray colormap shows the joint histogram.

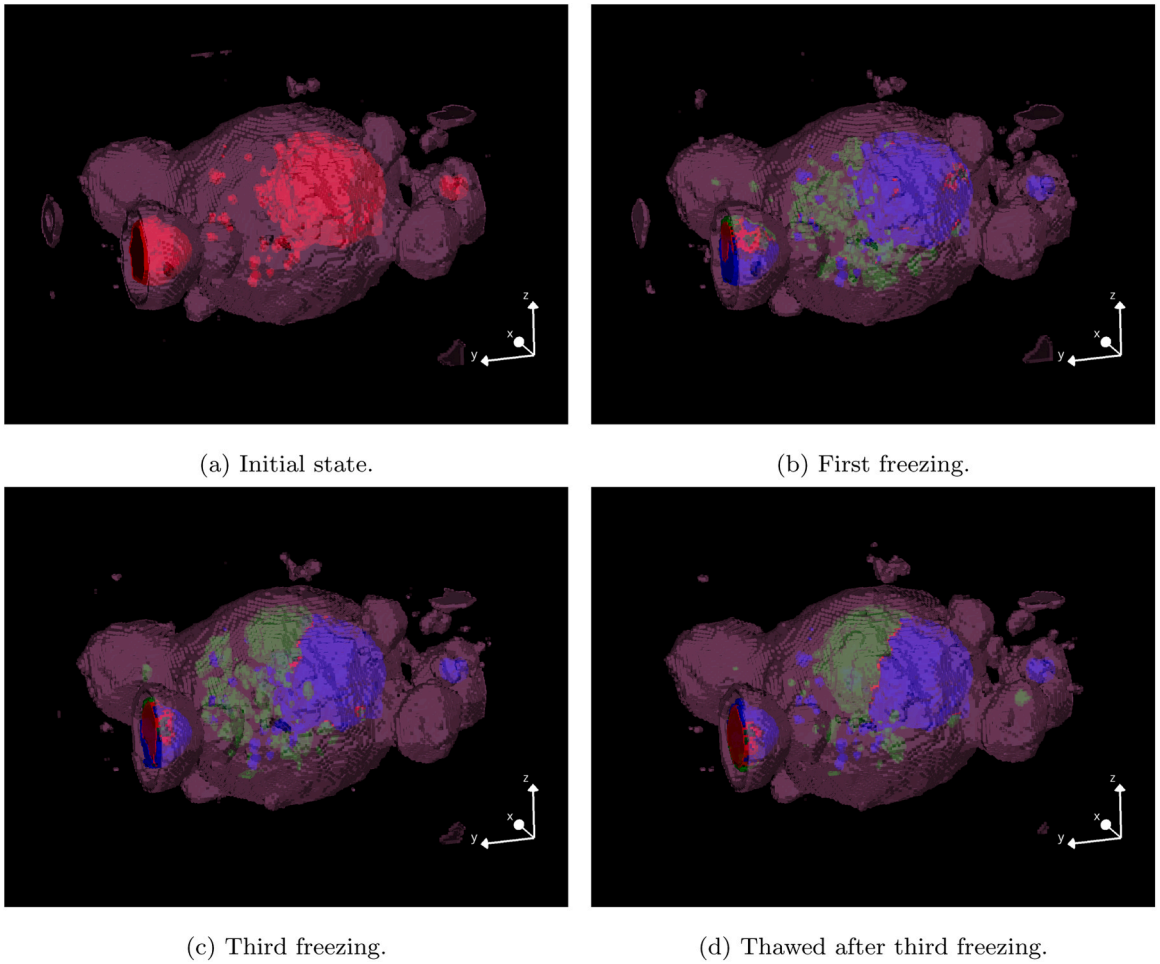

Fig. 5. Segmentation of a small porosity region in the concrete sample during freeze-thaw cycling. Pink, red, blue, and green correspond to water, air, air-to-water transition, and water-to-air transition regions, respectively. (a): In the initial, thawed state. (b): During the first freezing. (c): During the third freezing. (d): Thawed after the third freezing.

2.3. Identification of cluster positions

The most important step in the proposed segmentation method is identifying the number and position of clusters within the joint histogram. This can be achieved through manual inspection or by employing automatic methods. The *evoSegment* package supports both manual identification of cluster positions and implements two algorithms for automatic identification. The main algorithm is described below. Alternatively, clusters can be identified using a more general but harder-to-tune algorithm based on subtractive mountain clustering, described in appendix A. This method might be beneficial if the non-evolved portions of the images do not have the same grayscale value, i.e., there are no clusters along the main diagonal. This can happen if, e.g., the evolved image was taken inside some sample environment, causing the overall intensity to differ from the reference image, if the images were reconstructed using different settings, or if doing a local tomography and the whole region-of-interest evolves (for example by infiltration of contrast agents or water uptake).

2.3.1. Diagonal peak extraction

The diagonal peak extraction method is a phenomenological algorithm designed to identify clusters by leveraging some of the characteristics of the joint histogram. As mentioned above, the diagonal of the joint histogram contains information about the regions of the images that do not evolve. In most cases, microstructural evolution occurs in certain parts of the sample while leaving other parts unaffected. In terms of the joint histogram, this implies that there will be clusters of pixels along the diagonal, ideally one cluster for each material phase present in the sample. Microstructural evolution manifests as pixels shifting from diagonal to off-diagonal bins. It should be noted that this shift can only occur along the vertical axis in the joint histogram, meaning that the gray level can decrease, increase, or stay the same. Consequently, the off-diagonal clusters in the joint histogram must lie above or below the diagonal clusters.

Algorithm 1 provides a pseudo-code representation of the diagonal peak extraction method. The algorithm begins by extracting the diagonal from the joint histogram, with the option of including some sub- and super-diagonals (i.e., elements directly below or above the diagonal) to enhance the signal-to-noise ratio. Peaks in the extracted data are identified using peak finding methods from SciPy [35]. The identified peaks are integrated to determine how many image voxels belong to each peak. If the voxel count exceeds a supplied threshold value `kd`, the peak is accepted, and its position is stored as a cluster position.

Algorithm 1. Diagonal peak extraction.

Input : joint histogram array H

Input : Optional: *diagonalwidth*, *halfstripwidth*, *kd*, *ko*

Output: Number of detected cluster centers, Array of cluster center coordinates

$diag \leftarrow$ `sumDiagonalBand`$(H, diagonalwidth)$;

$diag\_peaks \leftarrow$ `findAndFilterPeaks`$(diag, kd)$;

$peaks \leftarrow$ empty list;

foreach p ***in*** $diag\_peaks$ **do**

  $strip \leftarrow H[:, p - halfstripwidth : p + halfstripwidth]$;

  $strip \leftarrow$ mean along rows;

  $odp \leftarrow$ `findAndFilterPeaks`$(strip, ko)$;

  if *odp is not empty* **then**

    append $[op, p]$ to $peaks$ for each op in odp;

return *Number of detected cluster centers, Array of cluster center coordinates*

Once all diagonal clusters are identified, the next step is to search for off-diagonal clusters. This is done by extracting a vertical strip around each diagonal peak and applying the same peak-finding procedure as for the diagonal peaks. The off-diagonal peaks are generally weaker than those on the diagonal. Therefore, a lower threshold value, `ko`, is used to accept off-diagonal peaks. The green crosses in Fig. 2 represent the peak positions identified using the diagonal peak extraction algorithm. Clearly, for this straightforward case, the cluster positions are correctly identified.

2.4. Labeling of clusters

Once the positions of the clusters are determined, the next step of the 4D segmentation is to assign labels to each bin in the joint histogram

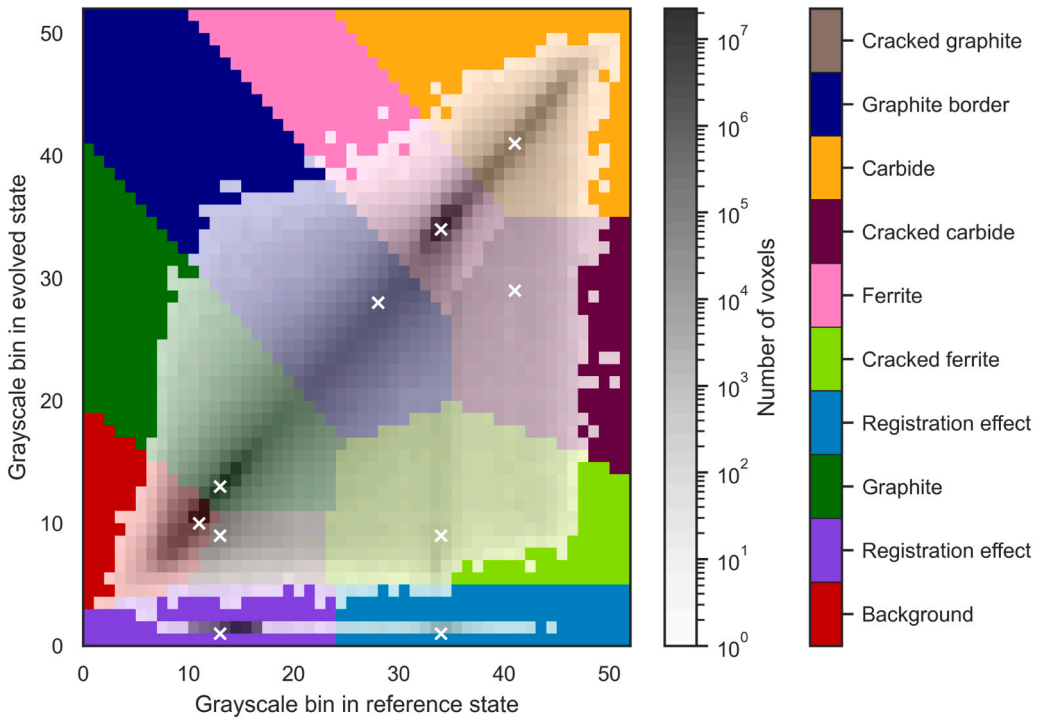

Fig. 6. Labeled joint histogram of the cast iron sample. The white crosses represent the cluster positions.

based on the proximity to the nearest cluster. Prior to labeling, one can optionally refine the cluster positions using k-means clustering of the histogram. The k-means clustering is a two-step algorithm. In the first step, each bin in the joint histogram is assigned a label based on the distance to the cluster positions. In the second step, the cluster positions are updated based on the center-of-mass position of the assigned labels. The two steps are repeated iteratively until the cluster positions become stationary.

Figure 3a shows the labeled histogram for the phantom example. The white crosses indicate the center-of-mass position of the labels obtained through clustering. A comparison between Fig. 3a and Fig. 2 reveals the accuracy of the segmentation. Each of the nonzero bins in the histogram is assigned a unique label, and the center-of-mass positions given by the clustering overlap with the non-empty bins in the histogram.

2.5. Mapping between histogram and image

The final step of the segmentation algorithm involves mapping the labeled histogram to the image of the sample. This is achieved by assigning each image voxel the label corresponding to its combination of grayscale values in the evolved and reference images. The segmented image of the Shepp-Logan phantom is shown in Fig. 3b. An interpretation of the labels is given in Table 1 to facilitate the evaluation of the segmentation results.

For datasets containing more than two images (e.g., the cement mortar dataset discussed below), it is advantageous to construct the joint histogram using a combination of all images for the evolved state. The most straightforward way is to use the reference image and the concatenation of all other images when building the joint histogram. This approach will ensure that all gray-level combinations present in the dataset are represented in the histogram. A notable advantage of this method is that the labeling of the histogram is performed only once, regardless of the number of time steps in the image sequence. The same labeling can then be used to map all time steps, as demonstrated in section 3.1.

3. Application examples

In this section, we demonstrate the application of the segmentation method presented above on two real datasets: water uptake in cement mortar during temperature cycling and damage evolution during tensile testing of a cast iron sample. Detailed analysis and discussion of these datasets will be presented in separate publications.

3.1. Water uptake in cement mortar

The first application example involves the segmentation of water and air exchange in the pore space in a cement mortar sample subjected to freeze-thaw cycling. The dataset was acquired using the X-ray source at the NeXT beamline at the Institut Laue-Langevin [36]. The experiment aimed to study the water uptake in cement mortar during cyclic freezing and thawing by combining neutron and X-ray imaging (only X-ray results are presented here). The sample was a 10 mm diameter cylinder of cement mortar, initially vacuum-saturated with water. After acquiring the first tomography, the sample was subjected to freeze-thaw cycling in situ at the beamline.

Figure 4a shows a reconstructed slice through the sample in its initial, unfrozen state. The (partially) water-filled pores are easily distinguishable from the mortar based on their circular shape and lower grayscale level. Upon closer inspection, dark regions can be observed within some of the pores. These indicate the presence of air, suggesting that the sample was not fully saturated with water at the start of the experiment (this was confirmed by the neutron imaging). The white annotation in Fig. 4a indicates the specific pore that will be further analyzed here. The physical size of the investigated subvolume is 1.5 mm $\times$ 1.65 mm $\times$ 1.0 mm.

The resulting labeling and the joint histogram are shown in Fig. 4b. The cluster detection was performed using the diagonal peak extraction method, which identified four diagonal and four off-diagonal clusters. The diagonal clusters correspond to air (red), water (light blue and pink), and cement mortar (orange). The water phase is represented by two clusters due to the slight difference in grayscale values between the edges and the interior of the pores. This discrepancy is most likely a

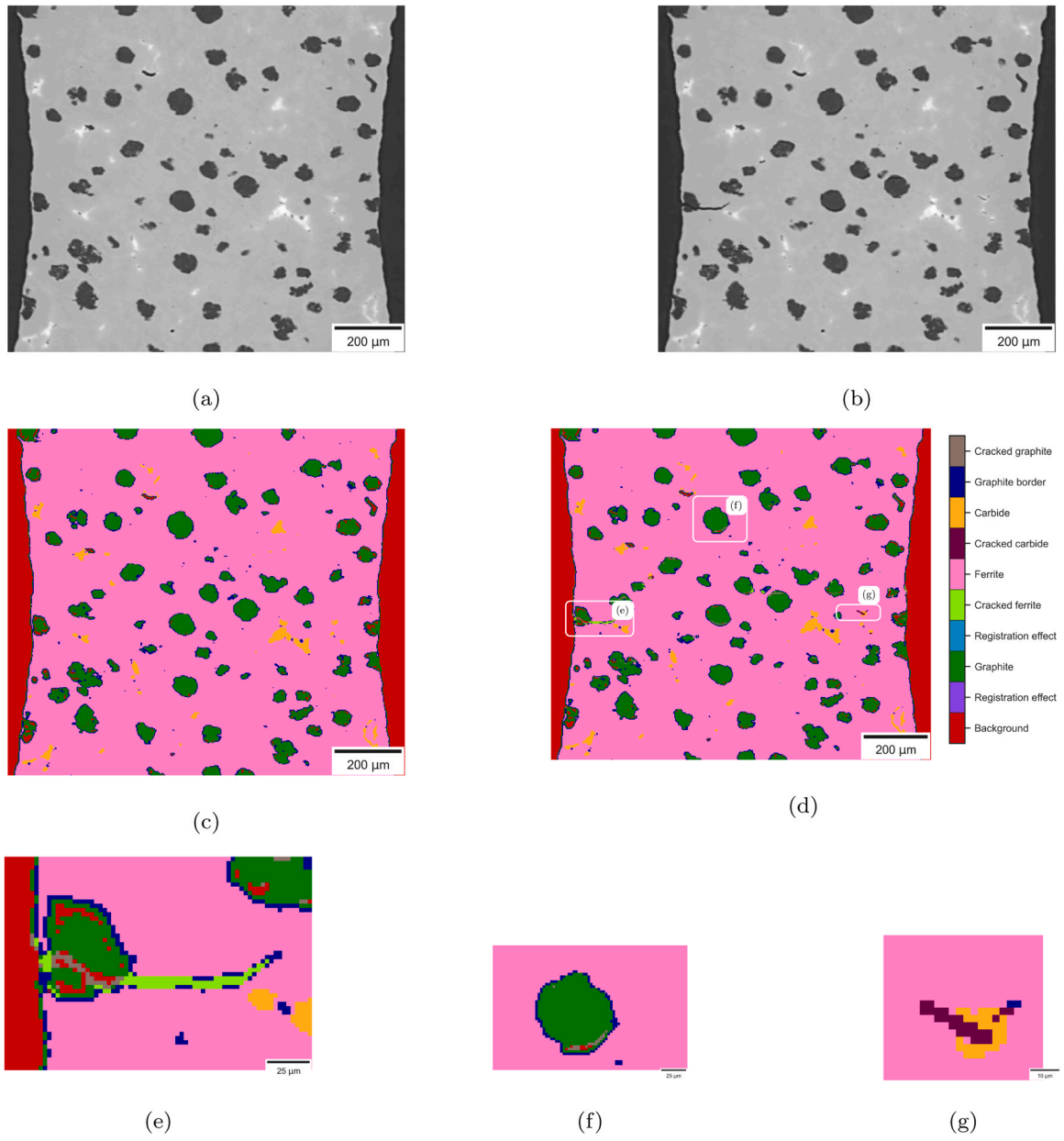

Fig. 7. Reconstructed slice through the cast iron sample and corresponding segmentation results at two load levels. The loading direction is vertical. (a): Reconstruction at 0 N. (b): Reconstruction at 640 N. (c): Segmentation at 0 N. (d): Segmentation at 640 N. The annotations denote the location of the regions shown in (e)-(g). (e): A crack originating in a graphite nodule at the surface and growing into the ferrite matrix. (f): A graphite nodule that is delaminating from the matrix. (g) A crack through a Mo-rich carbide.

phase-contrast effect that was not completely retrieved during reconstruction. It is, however, trivial to manually combine the pink and light blue clusters if necessary. The blue and green clusters represent voxels that change from air to water and vice versa between the reference and the evolved states, respectively. The two clusters at the bottom of the histogram (light green and dark purple) contain voxels that are cropped during the image registration process.

A 3D rendering of the selected pore, color-coded according to the labeled histogram, is shown in Fig. 5. To enhance the visibility of the water-air interaction, the mortar phase and the light blue water phase are set to be transparent. Figure 5a depicts the pore in its initial state before any freeze-thaw cycling. It is seen that most of the pore is filled with water, with a small amount of air present at the top of the pore. After the first freezing (Fig. 5b), most of the air has been replaced by water (the red color has transitioned to blue), and a few new small air bubbles (green) have formed. The newly formed air bubble seemingly grows slightly between the first and third freezing (Fig. 5c), and the growth continues during the thawing process, as observed in Fig. 5d. It should be emphasized that since the grayscale of the blue and the green phases in the evolved state are the same as those of the red and light blue phases, it would not be possible to separate these phases by thresholding of the evolved image alone.

3.2. *Damage evolution in cast iron*

The second example involves segmenting damage evolution in a cast iron sample during tensile testing. The dataset was obtained from an experiment conducted at beamline ID11 of the European Synchrotron

Radiation Facility (ESRF); for further details, see [37]. The experiment aimed to study deformation mechanisms and damage evolution in ductile cast iron samples during tensile deformation. An in situ tensile test of a cylindrical dog-bone tensile sample with a gauge diameter of 1.4 mm was performed. Phase-contrast X-ray tomography (PCT) was carried out at several predetermined load levels by interrupting the loading process. After reconstructing the PCT data, the volumes were registered to the reference volume by virtually deforming the images at each load step to match the reference volume. This was achieved using the software SPAM [34].

The joint histogram of the cast iron sample and the clustering result are shown in Fig. 6. In this case, the off-diagonal clusters are not as prominent as in the case of the cement mortar sample. Nevertheless, the diagonal peak extraction identifies several off-diagonal clusters corresponding to different types of damage evolution.

Figure 7a and b show a vertical slice through the sample at 0 N and 640 N load, respectively. From Fig. 7c, it is clear that the method successfully segments the primary phases of the cast iron sample. The pink label represents the ferritic matrix, the green label corresponds to graphite nodules, and the orange represents molybdenum-rich carbides. From Fig. 7d to g, it is seen that the off-diagonal clusters correspond to different damage mechanisms. Figure 7e provides a close-up view of a crack growing through a graphite nodule and into the ferritic matrix. Some of the pixels belonging to either the crack or the ferrite matrix have been wrongly classified as 'graphite border' (dark blue). This is due to the dark blue label extending too far below the pink label in Fig. 6. The remedy for such misclassifications is to either adjust the cluster positions, use a larger number of bins in the histogram to better separate the clusters, or use a more sophisticated criterion for assigning the bin labels. Similar issues can also be seen at the edges of the sample and in some of the graphite nodules. Note, however, that the part of the crack in the graphite and the matrix is correctly assigned different labels (gray and light green, respectively) due to the difference in grayscale values in the reference state. This distinction would not have been possible using conventional threshold-based segmentation methods. The ability to separate similar microstructure evolution in different primary phases allows for phase-specific quantification and, therefore, e.g., richer data to use for developing numerical models. In this particular case, it is, e.g., possible to easily determine the volume fractions of cracked graphite and cracked ferrite by analyzing the gray and light green labels independently. A crack (or delamination) between a graphite nodule and the matrix phase is also seen in Fig. 7f. In fact, most graphite nodules in Fig. 7d exhibit signs of delamination. Lastly, Fig. 7g shows crack growth (dark purple) in a molybdenum-rich carbide (orange).

4. Conclusions

A novel 4D segmentation algorithm based on the labeling of a joint histogram between a reference image and an image in an evolved state has been presented. The method was successfully applied to the segmentation of microstructural evolution from 4D X-ray tomography data of freeze-thaw cycling of a cement mortar and tensile deformation of cast iron samples. The method works by identifying clusters in the joint histogram, using, e.g., diagonal peak extraction, and assigning labels to the histogram bins based on these clusters. The labels are then mapped back to the image, resulting in accurate segmentation and characterization of the evolving microstructures. One of the main advantages of the method is that it will give phase-specific information about the grayscale evolution. In the case of the cast iron data, for example, this enabled the separation of cracks growing in graphite, carbides, and ferrite. Such details would be lost using standard thresholding. Another advantage is that only one labeling is needed to segment the whole image sequence regardless of the number of images. The examples shown involved X-ray tomography data, but the method is modality agnostic and can also be used for, e.g., dual-energy, spectral, or diffraction tomographies. The only requirement is that the images are spatially registered before the segmentation. The proposed method is implemented in the open-source Python package *evoSegment*.

CRediT authorship contribution statement

Engqvist Jonas: Investigation, Writing – review & editing. **Hall Stephen A.:** Conceptualization, Methodology, Writing – review & editing. **Hektor Johan:** Conceptualization, Formal analysis, Funding acquisition, Investigation, Methodology, Software, Visualization, Writing – original draft.

Declaration of Competing Interest

The authors declare that they have no known competing financial interests or personal relationships that could have appeared to influence the work reported in this paper.

Acknowledgements

The authors acknowledge the beamtime granted by ESRF (experiment number MA-5415) and ILL (experiment number UGA-101). This research was funded by the Knowledge Foundation (project ID 20190214), the Crafoord Foundation (project ID 20230630), Vinnova (project ID 2019-02556), and the QIM project at Lund University.

Appendix A. Subtractive mountain clustering

The subtractive mountain clustering algorithm [38,39] is based on computing the so-called clustering potential,

$$P(i) = \sum_{j=1}^{N} e^{-\alpha\left|\left|x_i - x_j\right|\right|^2}, \tag{A.1}$$

for each bin in the joint histogram. The parameter $\alpha = \frac{4}{r_a^2}$ controls the size of the influence region around each bin, and $||x_i - x_j||$ is the Euclidean distance between bins i and j. The clustering potential is highest for bins with many neighboring bins with high intensity values. The bin with the highest potential is selected as the first cluster position, u_0, and its associated potential $P(u_0) = P_0^*$ is taken as a reference potential for selecting further cluster positions. Once a cluster center u_n is selected, the clustering potential is updated according to

$$P(i) := P(i) - P(u_n)e^{-\beta\left|\left|x_i - u_n\right|\right|^2}, \tag{A.2}$$

where $\beta = \frac{4}{r_b^2}$ defines the size of the region affected by the reduction in potential. The constant r_b is typically set as $r_b = 1.5r_a$ to ensure that clusters are well-separated [40]. The reduction in clustering potential makes it unlikely for data points in close proximity to a selected cluster to be chosen as cluster centers. After reducing the potential of all bins, we again select the bin with the highest potential, P_n^*, as a cluster position and reduce the

potential of all bins based on the distance to the new cluster. This iterative procedure is repeated until the potential of all bins in the histogram is lower than a threshold value given by $\epsilon_b P_0^*$ with $0 < \epsilon_b < 1$.

References

[1] A.A. Martin, N.P. Calta, J.A. Hammons, S.A. Khairallah, M.H. Nielsen, R. M. Shuttlesworth, N. Sinclair, M.J. Matthews, J.R. Jeffries, T.M. Willey, J.R.I. Lee, Ultrafast dynamics of laser-metal interactions in additive manufacturing alloys captured by in situ X-ray imaging, Mater. Today Adv. 1 (2019), 100002, https://doi.org/10.1016/j.mtadv.2019.01.001. ⟨https://www.sciencedirect.com/science/article/pii/S2590049818300419⟩.

[2] B. Song, I. Dhiman, J.C. Carothers, G.M. Veith, J. Liu, H.Z. Bilheux, A. Huq, Dynamic lithium distribution upon dendrite growth and shorting revealed by operando neutron imaging (publisher: American Chemical Society), ACS Energy Lett. 4 (10) (2019) 2402–2408, https://doi.org/10.1021/acsenergylett.9b01652.

[3] S. Lou, N. Sun, F. Zhang, Q. Liu, J. Wang, Tracking Battery Dynamics by Operando Synchrotron X–ray imaging: operation from liquid electrolytes to solid-state electrolytes (publisher: american Chemical Society), Acc. Mater. Res. 2 (12) (2021) 1177–1189, https://doi.org/10.1021/accountsmr.1c00159.

[4] O.O. Taiwo, D.P. Finegan, J.M. Paz-Garcia, D.S. Eastwood, A.J. Bodey, C. Rau, S. A. Hall, D.J.L. Brett, P.D. Lee, P.R. Shearing, Investigating the evolving microstructure of lithium metal electrodes in 3D using X-ray computed tomography (publisher: Royal Society of Chemistry), Phys. Chem. Chem. Phys. 19 (33) (2017) 22111–22120, https://doi.org/10.1039/C7CP02872E (publisher: Royal Society of Chemistry), ⟨https://pubs.rsc.org/en/content/articlelanding/2017/cp/c7cp02872e⟩.

[5] P. Schad, M. Wollenweber, J. Thüring, J. Schock, J. Eschweiler, G. Palm, K. Radermacher, F. Eckstein, A. Prescher, C. Kuhl, D. Truhn, S. Nebelung, Magnetic resonance imaging of human knee joint functionality under variable compressive in-situ loading and axis alignment, J. Mech. Behav. Biomed. Mater. 110 (2020), 103890, https://doi.org/10.1016/j.jmbbm.2020.103890. ⟨https://www.sciencedirect.com/science/article/pii/S1751616120304446⟩.

[6] K. Madi, K.A. Staines, B.K. Bay, B. Javaheri, H. Geng, A.J. Bodey, S. Cartmell, A. A. Pitsillides, P.D. Lee, In situ characterization of nanoscale strains in loaded whole joints via synchrotron X-ray tomography, number: 3 Publisher: Nature Publishing Group, Nat. Biomed. Eng. 4 (3) (2020) 343–354, https://doi.org/10.1038/s41551-019-0477-1. number: 3 Publisher: Nature Publishing Group, ⟨https://www.nature.com/articles/s41551-019-0477-1⟩.

[7] S. LeCann, E. Tudisco, M. Tägil, S.A. Hall, H. Isaksson, Bone damage evolution around integrated metal screws using X-ray tomography — in situ pullout and digital volume correlation, Front. Bioeng. Biotechnol. 8 (2020), https://doi.org/10.3389/fbioe.2020.00934.

[8] F. Schott, S. Isaksson, E. Larsson, F. Marone, C. Öhgren, M. Röding, S. Hall, N. Lorén, R. Mokso, B.W. Raaholt, Structural formation during bread baking in a combined microwave-convective oven determined by sub-second in-situ synchrotron X-ray microtomography, Food Res. Int. 173 (2023), 113283, https://doi.org/10.1016/j.foodres.2023.113283. ⟨https://www.sciencedirect.com/science/article/pii/S0963996923008281⟩.

[9] S. Johansson, J. Engqvist, J. Tryding, S.A. Hall, Experimental investigation of microscale mechanisms during compressive loading of paperboard, Cellulose 30 (7) (2023) 4639–4662, https://doi.org/10.1007/s10570-023-05168-x.

[10] A. Wagih, M. Hasani, S.A. Hall, V. Novak, H. Theliander, In situ microstructural evolution of spruce wood during soda pulping using synchrotron X-ray tomography (publisher: De Gruyter), Holzforschung 76 (7) (2022) 611–621, https://doi.org/10.1515/hf-2021-0204.

[11] J.-P. Wang, J.-Y. Luan, X.-G. Gao, T.-H. Liu, E. Andò, B. François, A micro-investigation of unsaturated sand in mini-triaxial compression based on micro-CT image analysis, Acta Geotech. 17 (11) (2022) 4799–4821, https://doi.org/10.1007/s11440-022-01658-7.

[12] E. Tudisco, S.A. Hall, S. Athanasopoulos, J. Hovind, Neutron imaging and digital volume correlation to analyse the coupled hydro-mechanics of geomaterials, Riv. Ital. di Geotec. (2017).

[13] N. Otsu, A. Threshold, Selection method from gray-level histograms, IEEE Trans. Syst., Man, Cybern. 9 (1) (1979) 62–66.

[14] J. Canny, A computational approach to edge detection (conference Name: IEEE Transactions on Pattern Analysis and Machine Intelligence), IEEE Trans. Pattern Anal. Mach. Intell. PAMI 8 (6) (1986) 679–698, https://doi.org/10.1109/TPAMI.1986.4767851.

[15] M.S. Durkee, R. Abraham, M.R. Clark, M.L. Giger, Artificial intelligence and cellular segmentation in tissue microscopy images, Am. J. Pathol. 191 (10) (2021) 1693–1701, https://doi.org/10.1016/j.ajpath.2021.05.022. ⟨https://www.sciencedirect.com/science/article/pii/S0002944021002613⟩.

[16] H. Seo, M. BadieiKhuzani, V. Vasudevan, C. Huang, H. Ren, R. Xiao, X. Jia, L. Xing, Machine learning techniques for biomedical image segmentation: an overview of technical aspects and introduction to state-of-art applications, Med. Phys. 47 (5) (2020) e148–e167, https://doi.org/10.1002/mp.13649.

[17] S. Minaee, Y. Boykov, F. Porikli, A. Plaza, N. Kehtarnavaz, D. Terzopoulos, Image Segmentation Using Deep Learning: A Survey (conference Name: IEEE Transactions on Pattern Analysis and Machine Intelligence), IEEE Trans. Pattern Anal. Mach. Intell. 44 (7) (2022) 3523–3542, https://doi.org/10.1109/TPAMI.2021.3059968.

[18] M. YoitiItoParada, C. MatthiasSchlepütz, R. MichelRossi, D. Derome, J. Carmeliet, Two-stage wicking of yarns at the fiber scale investigated by synchrotron X-ray phase-contrast fast tomography (publisher: SAGE Publications Ltd STM), Text. Res. J. 89 (23-24) (2019) 4967–4979, https://doi.org/10.1177/0040517519843461.

[19] L.A. Shepp, B.F. Logan, The Fourier reconstruction of a head section, IEEE Trans. Nucl. Sci. 21 (3) (1974) 21–43, https://doi.org/10.1109/TNS.1974.6499235.

[20] C.-C. Chien, H.-H. Chen, S.-F. Lai, Y. Hwu, C. Petibois, C.S. Yang, Y. Chu, G. Margaritondo, X-ray imaging of tumor growth in live mice by detecting gold-nanoparticle-loaded cells, number: 1 Publisher: Nature Publishing Group, Sci. Rep. 2 (1) (2012) 610, https://doi.org/10.1038/srep00610. number: 1 Publisher: Nature Publishing Group, ⟨https://www.nature.com/articles/srep00610⟩.

[21] T.J. Heindel, J.N. Gray, T.C. Jensen, An X-ray system for visualizing fluid flows, Flow. Meas. Instrum. 19 (2) (2008) 67–78, https://doi.org/10.1016/j.flowmeasinst.2007.09.003. ⟨https://www.sciencedirect.com/science/article/pii/S0955598607000763⟩.

[22] A. Janzen, J. Steube, S. Aferka, E.Y. Kenig, M. Crine, P. Marchot, D. Toye, Investigation of liquid flow morphology inside a structured packing using X-ray tomography, Chem. Eng. Sci. 102 (2013) 451–460, https://doi.org/10.1016/j.ces.2013.08.035. ⟨https://www.sciencedirect.com/science/article/pii/S0009250913005782⟩.

[23] T. Hirono, M. Takahashi, S. Nakashima, In situ visualization of fluid flow image within deformed rock by X-ray CT, Eng. Geol. 70 (1) (2003) 37–46, https://doi.org/10.1016/S0013-7952(03)00074-7. ⟨https://www.sciencedirect.com/science/article/pii/S0013795203000747⟩.

[24] A. Aliseda, T.J. Heindel, X-ray flow visualization in multiphase flows, Annu. Rev. Fluid Mech. 53 (1) (2021) 543–567, https://doi.org/10.1146/annurev-fluid-010719-060201.

[25] F. Renard, D. Bernard, J. Desrues, A. Ougier-Simonin, 3D imaging of fracture propagation using synchrotron X-ray microtomography, Earth Planet. Sci. Lett. 286 (1) (2009) 285–291, https://doi.org/10.1016/j.epsl.2009.06.040. ⟨https://www.sciencedirect.com/science/article/pii/S0012821×09003811⟩.

[26] W. Qian, S. Wu, Z. Wu, S. Ahmed, W. Zhang, G. Qian, P.J. Withers, In situ X-ray imaging of fatigue crack growth from multiple defects in additively manufactured AlSi10Mg alloy, Int. J. Fatigue 155 (2022), 106616, https://doi.org/10.1016/j.ijfatigue.2021.106616. ⟨https://www.sciencedirect.com/science/article/pii/S014211232100462X⟩.

[27] N. Kouraytem, P.-J. Chiang, R. Jiang, C. Kantzos, J. Pauza, R. Cunningham, Z. Wu, G. Tang, N. Parab, C. Zhao, K. Fezzaa, T. Sun, A.D. Rollett, Solidification crack propagation and morphology dependence on processing parameters in AA6061 from ultra-high-speed x-ray visualization, Addit. Manuf. 42 (2021), 101959, https://doi.org/10.1016/j.addma.2021.101959. ⟨https://linkinghub.elsevier.com/retrieve/pii/S221486042100124X⟩.

[28] J.M. Paz-Garcia, O.O. Taiwo, E. Tudisco, D.P. Finegan, P.R. Shearing, D.J.L. Brett, S.A. Hall, 4D analysis of the microstructural evolution of Si-based electrodes during lithiation: time-lapse X-ray imaging and digital volume correlation, J. Power Sources 320 (2016) 196–203, https://doi.org/10.1016/j.jpowsour.2016.04.076. ⟨https://www.sciencedirect.com/science/article/pii/S0378775316304396⟩.

[29] E. Törnquist, S. LeCann, E. Tudisco, A. Tengattini, E. Andò, N. Lenoir, J. Hektor, D. B. Raina, M. Tagil, S.A. Hall, Dual modality neutron and x-ray tomography for enhanced image analysis of the bone-metal interface, Phys. Med. Biol. (2021), https://doi.org/10.1088/1361-6560/ac02d4.

[30] J. Martell, C. Alwmark, L. Daly, S. Hall, S. Alwmark, R. Woracek, J. Hektor, L. Helfen, A. Tengattini, M. Lee, The scale of a martian hydrothermal system explored using combined neutron and x-ray tomography, eabn3044, Sci. Adv. 8 (19) (2022), https://doi.org/10.1126/sciadv.abn3044.

[31] E. Tudisco, C. Jailin, A. Mendoza, A. Tengattini, E. Andò, S.A. Hall, G. Viggiani, F. Hild, S. Roux, An extension of digital volume correlation for multimodality image registration (publisher: IOP Publishing), Meas. Sci. Technol. 28 (9) (2017), 095401, https://doi.org/10.1088/1361-6501/aa7b48.

[32] A.P. Kaestner, J. Hovind, P. Boillat, C. Muehlebach, C. Carminati, M. Zarebanadkouki, E.H. Lehmann, Bimodal Imaging at ICON Using Neutrons and X-rays, Phys. Procedia 88 (2017) 314–321, https://doi.org/10.1016/j.phpro.2017.06.043. ⟨https://www.sciencedirect.com/science/article/pii/S1875389217300937⟩.

[33] B. Zitová, J. Flusser, Image registration methods: a survey, Image Vis. Comput. 21 (11) (2003) 977–1000, https://doi.org/10.1016/S0262-8856(03)00137-9. ⟨https://www.sciencedirect.com/science/article/pii/S0262885603001379⟩.

[34] O. Stamati, E. Andò, E. Roubin, R. Cailletaud, M. Wiebicke, G. Pinzon, C. Couture, R.C. Hurley, R. Caulk, D. Caillerie, T. Matsushima, P. Besuelle, F. Bertoni, T. Arnaud, A.O. Laborin, R. Rorato, Y. Sun, A. Tengattini, O. Okubadejo, J.-B. Colliat, M. Saadatfar, F.E. Garcia, C. Papazoglou, I. Vego, S. Brisard, J. Dijkstra, G. Birmpilis, Spam: software for practical analysis of materials, J. Open Source Softw. 5 (51) (2020) 2286, https://doi.org/10.21105/joss.02286. ⟨https://hal.univ-grenoble-alpes.fr/hal-03020460⟩.

[35] P. Virtanen, R. Gommers, T.E. Oliphant, M. Haberland, T. Reddy, D. Cournapeau, E. Burovski, P. Peterson, W. Weckesser, J. Bright, S.J. van der Walt, M. Brett, J. Wilson, K.J. Millman, N. Mayorov, A.R.J. Nelson, E. Jones, R. Kern, E. Larson, C. J. Carey, I. Polat, Y. Feng, E.W. Moore, J. VanderPlas, D. Laxalde, J. Perktold, R. Cimrman, I. Henriksen, E.A. Quintero, C.R. Harris, A.M. Archibald, A.H. Ribeiro, F. Pedregosa, P. van Mulbregt, SciPy 1.0: fundamental algorithms for scientific computing in Python, number: 3 Publisher: Nature Publishing Group, Nat. Methods 17 (3) (2020) 261–272, https://doi.org/10.1038/s41592-019-0686-2. number: 3

Publisher: Nature Publishing Group, ⟨https://www.nature.com/articles/s41592%E2%80%90019%E2%80%900686%E2%80%902⟩.

[36] A. Tengattini, N. Lenoir, E. Andò, B. Giroud, D. Atkins, J. Beaucour, G. Viggiani, NeXT-grenoble, the neutron and X-ray tomograph in grenoble, nuclear instruments and methods in physics research section a: accelerators, spectrometers, Detect. Assoc. Equip. 968 (2020), 163939, https://doi.org/10.1016/j.nima.2020.163939. ⟨https://linkinghub.elsevier.com/retrieve/pii/S0168900220304198⟩.

[37] J. Senaneuch, J. Hektor, J. Engqvist, L. Elmquist, P. Skoglund, Understanding damage evolution in silicon-molybdenum alloyed cast iron through 3D imaging on multiple length scales (2025). 10.15151/ESRF-ES-928801822.

[38] S.L. Chiu, Fuzzy model identification based on cluster estimation (publisher: IOS Press), J. Intell. Fuzzy Syst. 2 (3) (1994) 267–278, https://doi.org/10.3233/IFS-1994-2306 (publisher: IOS Press), ⟨https://content.iospress.com/articles/journal-of-intelligent-and-fuzzy-systems/ifs2-3-06⟩.

[39] A. Chmielowiec, Implementation of the Mountain Clustering Method and Comments on its Practical use for Determining Cluster Centers, Oficyna Wydawnicza Politechniki Rzeszowskiej, 2019, accepted: 2020–05-04T11:15:53Z.⟨https://depot.ceon.pl/handle/123456789/18295⟩.

[40] S. Chiu, A cluster estimation method with extension to fuzzy model identification, In: Proceedings of 1994 IEEE 3rd International Fuzzy Systems Conference, 1994, 1240–1245, vol. 2. 10.1109/FUZZY.1994.343644.